

Title	Charpy absorbed energy in simulated heat-affected zone of laser-arc hybrid welded joints by high-strength steel for bridge structures
Author(s)	Chen, Gang; Hirohata, Mikihiro; Sakai, Natsumi et al.
Citation	International Journal of Advanced Manufacturing Technology. 2023, 127, p. 2655-2669
Version Type	VoR
URL	<a href="https://hdl.handle.net/11094/92498">https://hdl.handle.net/11094/92498</a>
rights	This article is licensed under a Creative Commons Attribution 4.0 International License.
Note	

***Osaka University Knowledge Archive : OUKA***

<https://ir.library.osaka-u.ac.jp/>

Osaka University



# Charpy absorbed energy in simulated heat-affected zone of laser-arc hybrid welded joints by high-strength steel for bridge structures

Gang Chen<sup>1</sup> · Mikihiro Hirohata<sup>1</sup> · Natsumi Sakai<sup>1</sup> · Kengo Hyoma<sup>2</sup> · Naoyuki Matsumoto<sup>2</sup> · Koutarou Inose<sup>2</sup>

Received: 16 December 2022 / Accepted: 6 April 2023 / Published online: 5 June 2023  
© The Author(s) 2023

## Abstract

The application of laser-arc hybrid welding (so-called, hybrid welding) to the fabrication of steel bridge members has recently been investigated. One-pass full-penetration butt joints of steels for bridge high-performance structure (SBHS400 and SBHS500) with a thickness of 15 mm were performed by hybrid welding. The sound butt joints by hybrid welding were confirmed by a series of tests. The Charpy impact test was performed on the test pieces extracted from the hybrid welded butt joints with specified test temperatures. A phenomenon known as fracture path deviation (FPD) occurred in most test pieces, due to a large variation in material properties of the heat-affected zone (HAZ), resulting in the difficulty of estimating the toughness of HAZ in hybrid welded joints. Therefore, the Charpy impact test was conducted on the test pieces subjected to the welding thermal cycle tests of hybrid welding, which can exclude the heterogeneity of material properties and obtain the Charpy absorbed energy of the HAZ with high accuracy. The test results indicated that FPD was not observed in all thermal cycle simulated test pieces because the uniform metallographic structures in the vicinity of the notch were formed by the simulated thermal cycle tests, and all thermal cycle simulated test pieces satisfied 47 J at the specified test temperatures, a value that prevents brittle fracture for SBHS. Besides, for investigating the effect of the high Charpy absorbed energy guaranteed by SBHS on the toughness of hybrid welded joints, the Charpy absorbed energy of the thermal cycle simulated test pieces of SBHS and those of conventional steel (SM400B) were compared. The results showed that some of the thermal cycle simulated test pieces of SM400B failed to satisfy 27 J, suggesting that SBHS may ensure a Charpy absorbed energy of 47 J or more in the HAZ of hybrid welded joints.

**Keywords** Laser-arc hybrid welding · Steels for bridge high performance structures · Butt-welded joints · Simulated thermal cycle test · Charpy impact test

## 1 Introduction

Welded connections are widely employed for joining and assembling steel structural members, along with bolted connections. Arc welding, as a method of welded connections, is the most extensively utilized because of its low equipment costs and high reliability based on technical accumulation for many years. On the other hand, laser welding, which uses a laser beam as a heat source, has been attracting attention as a welding method for steel structures in recent years. Laser

welding features high speed and deep penetration that cannot be achieved by arc welding in that the high energy density generated by laser beams is concentrated in a narrow area. Moreover, the total heat input is decreased because of the reduction in welding passes and welding time. And it is also effective in suppressing welding deformation [1]. Nevertheless, the gap between steel plates to be joined should be severely controlled since laser welding employs laser beams as the heat source to melt part of steel plates and join them together. Otherwise, welding defects are generated, such as underfill and melt-through [2]. Furthermore, the high energy density concentrated in narrow areas can cause hardening and welding cracks due to the rapid heating and cooling of welds, making the selection of proper welding conditions a challenge.

In order to resolve these challenges caused by laser welding, a series of investigations have been conducted on the

✉ Mikihiro Hirohata  
hirohata@civil.eng.osaka-u.ac.jp

<sup>1</sup> Graduate School of Engineering, Osaka University, Osaka, Japan

<sup>2</sup> IHI Corporation, Tokyo, Japan

**Table 1** Chemical compositions

Material	Chemical compositions (mass%)								
	C	Si	Mn	P	S	Ni	Cr	Fe	
SBHS400	0.11	0.29	1.36	0.009	0.001	0.01	0.02	bal	
SBHS500	0.10	0.24	1.57	0.008	0.003	0.02	0.12	bal	
G49AP3M16	0.08	0.71	1.21	0.01	0.007	—	—	bal	

application of laser-arc hybrid welding (so-called, hybrid welding) [3–6], a welding process combining arc and laser as heat sources. Hybrid welding takes advantage of the merits of laser welding, such as high speed and deep penetration. Meanwhile, compared to only laser welding, the gap tolerance is widened on account of the supplement of deposit metals from arc welding and then welding defects are reduced. In addition, the total heat input is decreased compared to only arc welding, which is expected to suppress welding deformation [7].

On the other hand, high-yield-point steel plates for bridges (SBHS: steels for bridge high-performance structure) with excellent strength, workability, and weldability have been developed and are expected to rationalize structures, improve manufacturing efficiency, reduce construction costs, and upgrade reliability [8]. While novel design concepts and structural types have been investigated to extend the application of SBHS [9, 10], the research is being investigated on the application of hybrid welded joints by SBHS to steel bridge members as a combination of new materials and new joining methods from the viewpoint of enhancing the manufacturing efficiency and reliability of welded joints. In a previous study [8], the authors explored welding conditions to fabricate one-pass full-penetration butt joints by hybrid welding for SBHS400 with a plate thickness of 15 mm. Tensile, bending, and Vickers hardness tests were performed on the test pieces extracted from the fabricated hybrid welded joints [11]. The results indicated that the tensile strength characteristics and sufficient bending properties of the hybrid welded joints by SBHS satisfied the criteria of base metals. However, the toughness of the laser welded or the hybrid welded joints is not easy to be examined because of the narrow heat-affected zone (HAZ) in which significant

hardening occurs by rapid heating and cooling during hybrid welding. The previous study showed that fracture path deviation (FPD) occurred from the V-shaped notch root set in the narrow weld metal and HAZ to base metals [12]. Accordingly, the characteristics of Charpy absorbed energy of the hybrid welded joints have not been investigated sufficiently. In this study, Charpy impact tests were performed on the simulated HAZ of hybrid welded joints of SBHS by extracting test pieces from the same materials whose metallographic structures of the actual HAZ were roughly reproduced by simulated thermal cycle tests. The influence of the thermal history of hybrid welding on the metallurgical properties of SBHS was examined, and the characteristics of Charpy absorbed energy in the simulated HAZ of hybrid welded joints by SBHS were discussed.

## 2 Material and experimental procedures

### 2.1 Material

The materials used to fabricate hybrid welded joints were SBHS400 and SBHS500. The chemical compositions and mechanical properties of materials and welding wire used in this study are shown in Tables 1 and 2 (mill sheet values and catalog values). The thickness of the specimens was 16 mm. The type of welding wire is G49AP3M16, specified by JIS Z 3312. The wire diameter was 1.2 mm. Additionally, the materials employed to make simulated HAZ test pieces were SBHS400, SBHS500, and SM400B. SM400B, a rolled steel for welded structures, was used as the conventional steel and its mechanical properties and Charpy absorbed energy are shown in Table 2.

**Table 2** Mechanical properties and Charpy absorbed energy

Material	Yield strength (MPa)	Tensile strength (MPa)	Elongation (%)	Charpy absorbed energy	
				Test temperatures (degree)	Charpy absorbed energy (J)
SBHS400	503	567	22	0	280
SBHS500	559	643	35	-5	274
G49AP3M16	490	590	31	—	—
SM400B	300	448	29	0	185

## 2.2 Charpy impact test of hybrid welded joints

### 2.2.1 Fabrication of hybrid welded joints

For fabricating hybrid welded joints using SBHS400 and SBHS500, the experimental specimens were manufactured to the shape and dimensions illustrated in Fig. 1 [11]. To suppress a misalignment caused by tack welding, with reference to previous research [13], hybrid welding was performed in the 0.3 mm wide slit set in the center of one steel plate, instead of being assembled with two steel plates. Protruding tabs were set from the start and end of the weld line with 340 mm in length. The thickness of the steel plates became 15 mm because the mill scale was removed from the obverse and reverse surfaces of the steel plate, within the range of 50 mm width centered on the slit.

One-pass full-penetration welding for butt joints with 15 mm in thickness could be performed without any welding defects under the following welding conditions: arc current of 255 A to 258 A, arc voltage of 28 V, laser power of 13 kW, and speed of 1.6 m/min, based on results obtained from a series of investigations to search for appropriate welding conditions that prevent welding defects and cracking [8]. Figure 2 shows macroscopic photographs of the welded part. Test specimens were extracted from the welded joints and subjected to tensile and bending tests. The results showed that the tensile

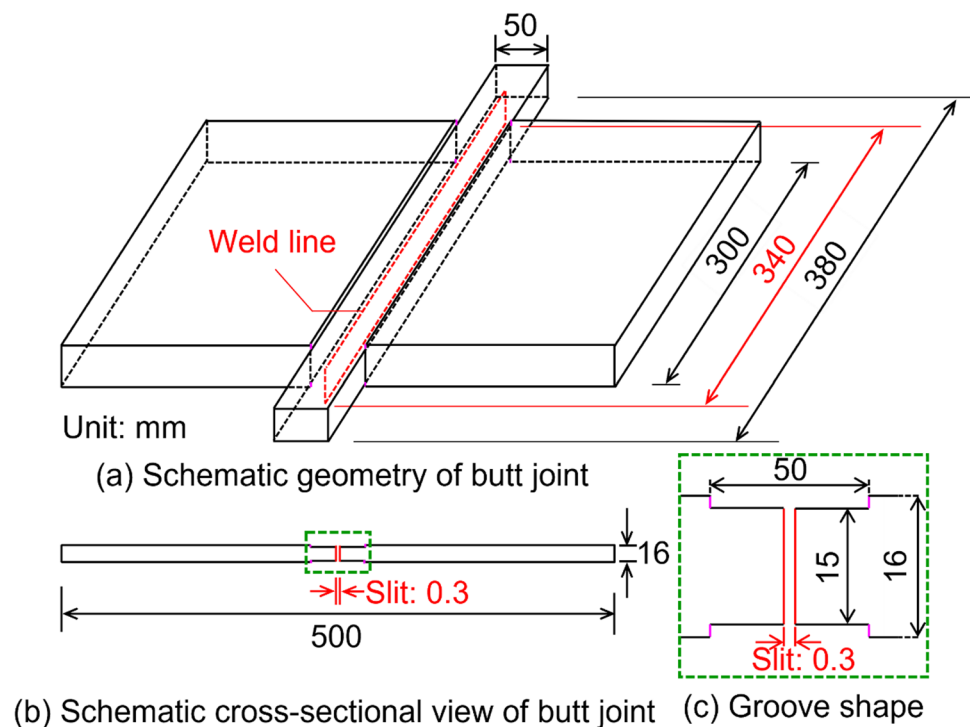
properties of welded joints met the specifications of base metals. Moreover, no welding cracks and defects were observed from the results of the face bend, root bend, and side bend tests, as well as even 180-degree bending [11].

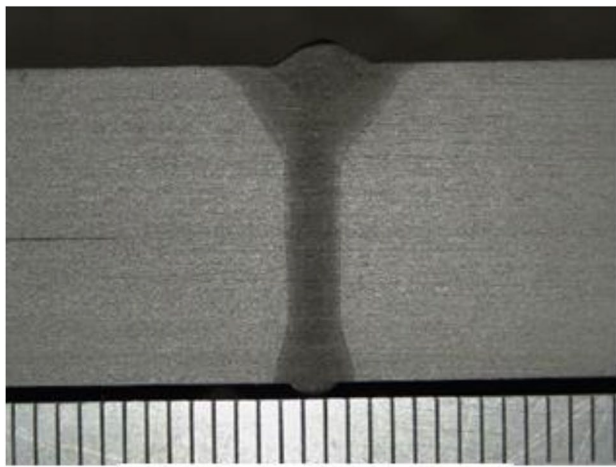
Figure 3 shows the results of Vickers hardness tests on the welded part performed in our previous study [8]. The hardness in the weld metal and HAZ of hybrid-welded joints dramatically increased due to the rapid heating and cooling within a narrow area compared to conventional arc welding. The hardened area was narrow at the midspan in the thickness direction.

### 2.2.2 Test piece for Charpy impact test

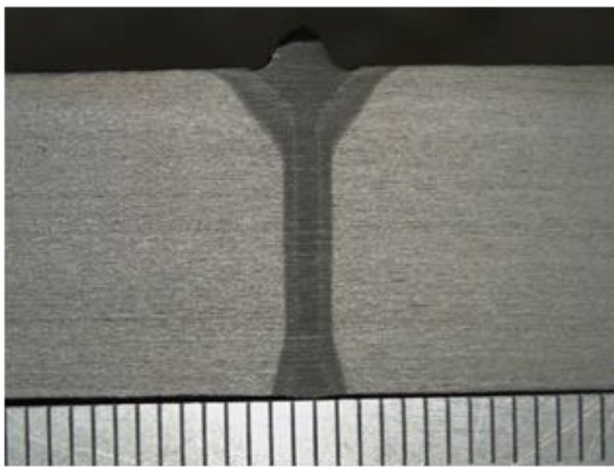
Test pieces for Charpy impact tests were sampled from the weld metal, central HAZ, and base metal of hybrid welded joints with SBHS400 and SBHS500. There are three test pieces for each type. Charpy impact tests were performed on these test pieces. The No. 4 test piece with a V-shaped notch was adopted, which is specified by JIS Z 2242. Figure 4 illustrates the shape and dimensions of the test pieces for the Charpy impact test. The Charpy probe was parallel to the weld seam. The V-shaped notch was installed to the central HAZ for the test pieces of HAZ. In the same way, the notch was installed to the central weld metal for the test piece of weld metal. The test temperatures for test pieces of SBHS400 and SBHS500 were 0 °C and –5 °C specified by JIS, respectively.

**Fig. 1** Shape and dimensions of welded joints





(a) SBHS400



(b) SBHS500

Fig. 2 Macroscopic photographs of welded part

## 2.3 Charpy impact test of thermal cycle simulated test pieces

### 2.3.1 Simulated welding thermal cycle test

It has been reported in previous studies that the Charpy impact test on laser welded joints whose weld metal is as narrow as the weld metal of hybrid welded joints causes a phenomenon called fracture path deviation (FPD), where a crack originating from the weld metal deviates to the base metal [12, 14, 15]. The occurrence of FPD was anticipated in the Charpy impact test on the hybrid welded joints in this study. Actually, almost all specimens of which the V-notch was at the weld metal or HAZ showed FPD in the Charpy impact test described later. To prevent the occurrence of FPD and obtain effective Charpy absorbed energy, the material of the specimen should not be changed in the narrow area but should be uniform. Therefore, simulated welding thermal cycle tests were conducted for creating the uniform material from which the Charpy impact test specimens were extracted.

The equipment used in this study was the THERMECMASTOR-Z made by Fuji Electronic Industrial Co., Ltd. The heating method was high-frequency induction heating, and cooling was performed by helium gas injection. The temperature was controlled by thermocouples attached to the center of the test pieces. The maximum heating temperatures were 1350 °C, 1200 °C, 1050 °C, and 900 °C. The temperatures were kept for 5 s and then cooled at 80 °C/s which was the maximum cooling rate by the equipment. The cooling rate of the hybrid welding varies with the welding conditions and the thickness of the plates to be joined. It was difficult to identify the cooling rate for simulating HAZ of the hybrid welded joints. A previous study of hybrid welding on steel plates 4.8 mm thick showed that the cooling rate in the fusion zone was calculated as 20–83.3 °C/s [16]. In the case of another previous study of hybrid welding

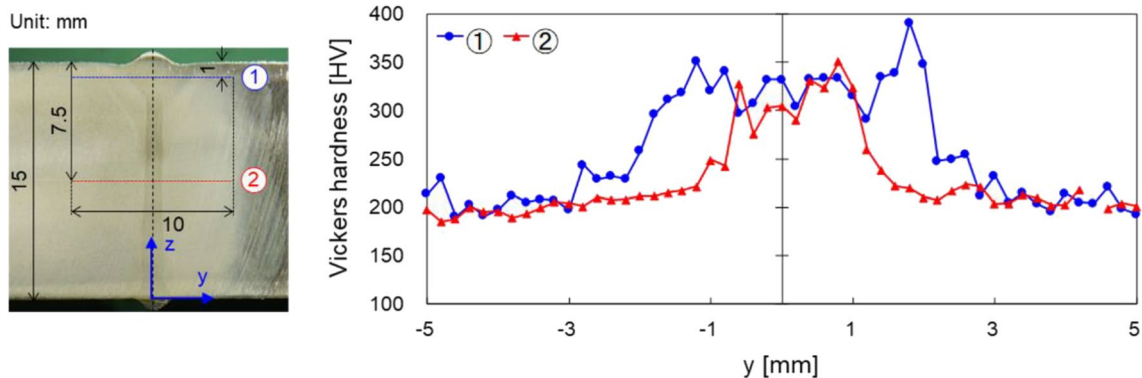
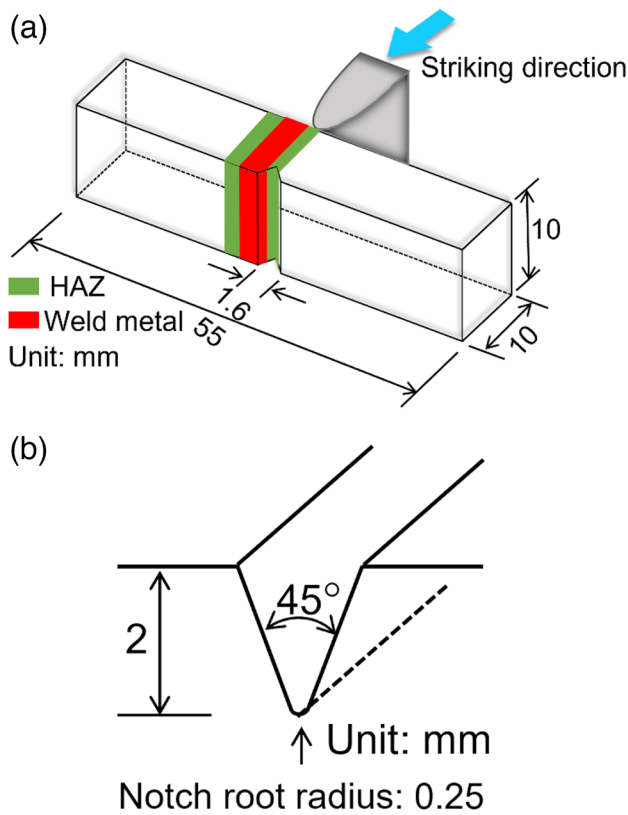


Fig. 3 Results of Vickers hardness test



**Fig. 4** An example of schematic geometry of test piece. **a** Shape and dimensions of test pieces. **b** V-shaped notch

on steel plates 6 mm thick, the cooling rate in HAZ was 25–35 °C/s [17]. The cooling rate selected in this study seemed to be within these values.

The materials of SBHS400, SBHS500, and SM400B were subjected to thermal histories by simulated thermal cycle tests (maximum heating temperatures of 1350 °C, 1200 °C, 1050 °C, and 900 °C, and a cooling rate of 80 °C/s). The dimensions of simulated materials are 120×12×12 mm. The Charpy impact test pieces were extracted from these thermal cycle simulated materials with the same geometry and dimensions as the No. 4 test piece illustrated in Sect. 2.2.2. There are three simulated test pieces for each type. The simulated welding thermal cycle test can reproduce the thermal cycles that the base metal undergoes during welding, and can simulate the metallurgical structures of the HAZ generated by welding as a uniform material. By obtaining the Charpy impact test pieces from the thermal cycle simulated materials, the heterogeneity of material properties can be excluded and the Charpy absorbed energy of the HAZ can be estimated with high accuracy. It should be noted, however, that the simulated thermal cycle tests cannot simulate the microstructures of weld metals because simulated materials cannot be melted, and only the HAZ can be simulated.

**2.3.2 Metallographic observation and Vickers hardness test**

As shown in Fig. 5, concerning the metallographic structure of the actual HAZ, three views were photographed at 500× magnification, starting with the region adjacent to the weld metal, and the regions were designated as region ① (coarse-grained HAZ), region ② (midspan in HAZ), and region ③ (fine-grained HAZ). For comparing the metallographic structure of the actual HAZ and simulated HAZ, the metallographic structure of the simulated HAZ was also photographed

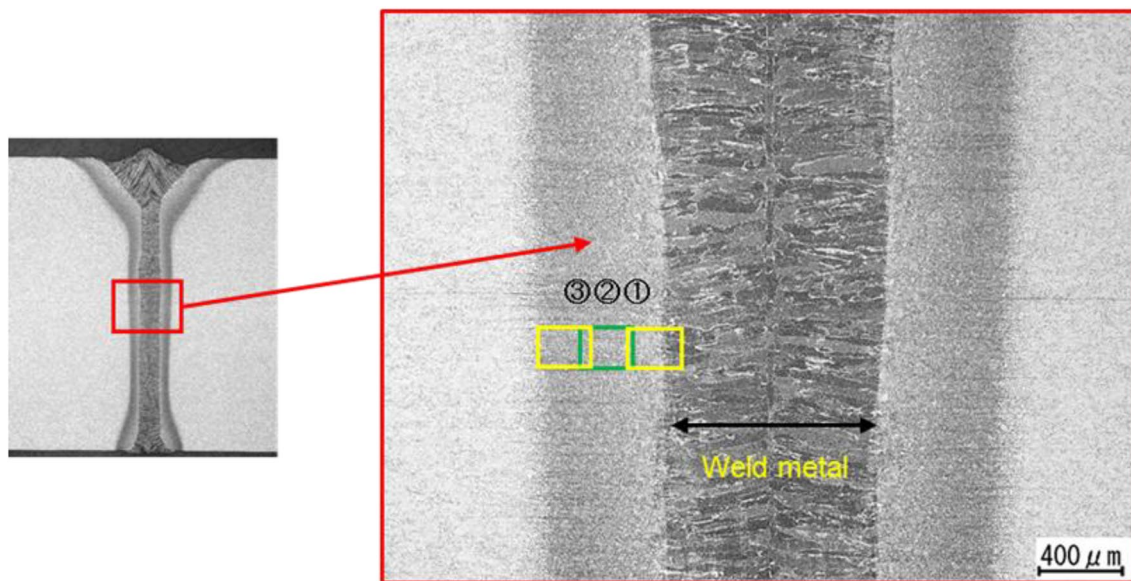


**Fig. 5** Metallographic observation location for hybrid welded joint

at  $500\times$  magnification. In this study, the fraction of coarsened metallographic structures was measured by the image analysis software WinROOF2018.

Hardness, as well as the fraction of coarsened metallographic structures, is a significant index in evaluating the similarity of metallographic structures, so the hardness of each specimen was measured by Vickers hardness tests.

### 2.3.3 Charpy impact test of thermal cycle simulated test piece

The Charpy impact test was performed on the simulated test pieces illustrated in Sect. 2.3.1. The test temperatures were  $0\text{ }^{\circ}\text{C}$  for SBHS400 and SM400B, and  $-5\text{ }^{\circ}\text{C}$  for SBHS500 specified by JIS.

## 3 Results

### 3.1 Charpy impact test of welded joints

#### 3.1.1 Charpy absorbed energy

Figure 6 demonstrates the Charpy absorbed energy of each part in hybrid welded joints for SBHS400 and SBHS500. Solid and dotted lines show the specified value (100 J) of Charpy absorbed energy for base metals and the average values of Charpy absorbed energy for base metals obtained from the tests. The numbers (1, 2, and 3) in the figure represent the test piece numbers. In this test, the average Charpy absorbed energy of base metals was 294 J for SBHS400 and 269 J for SBHS500, approximately 2.9 and 2.7 times higher than the specified value (100 J) for the base metals. For the weld metal and HAZ, the Charpy absorbed energy was equivalent to that of the base metal for all test pieces except the test piece of SBHS500 in the HAZ (test piece symbol: 5H2, an abbreviation for SBHS500, HAZ, and No. 2). The absorbed energy of the test piece 5H2 was 82 J.

#### 3.1.2 Fracture status and brittle fracture surface ratio

Figure 7 shows the fracture states of the test pieces for SBHS400 and SBHS500. The decrease in Charpy absorbed energy was observed only in the test piece 5H2, where a crack did not deviate from the notch root and propagated straight, indicating that brittle fracture was dominant, and a relatively large number of brittle fracture surfaces were observed. The brittle fracture surface ratio of other test pieces was almost 0%.

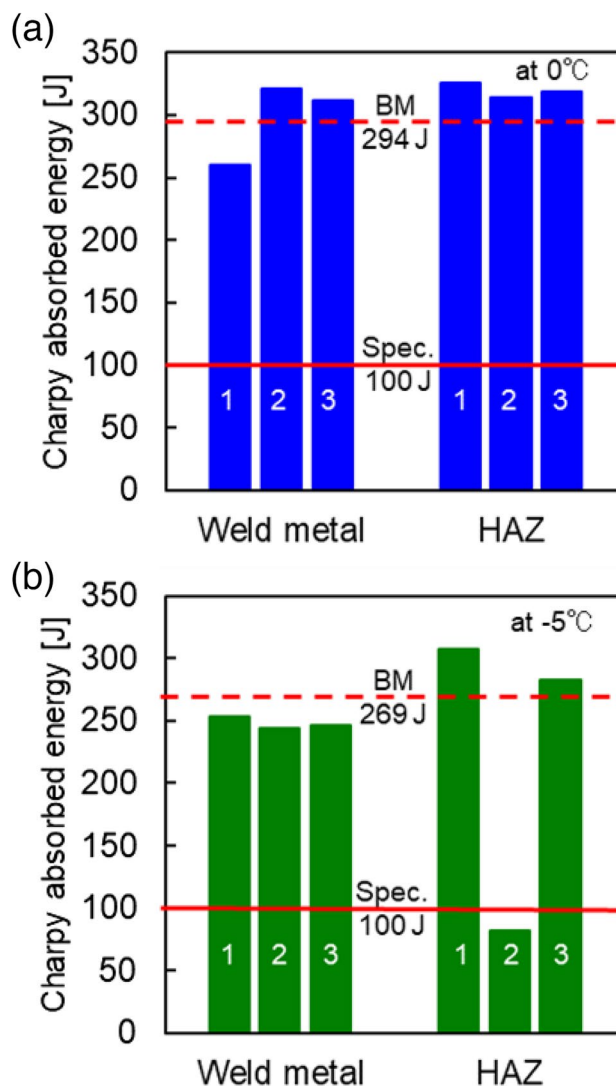
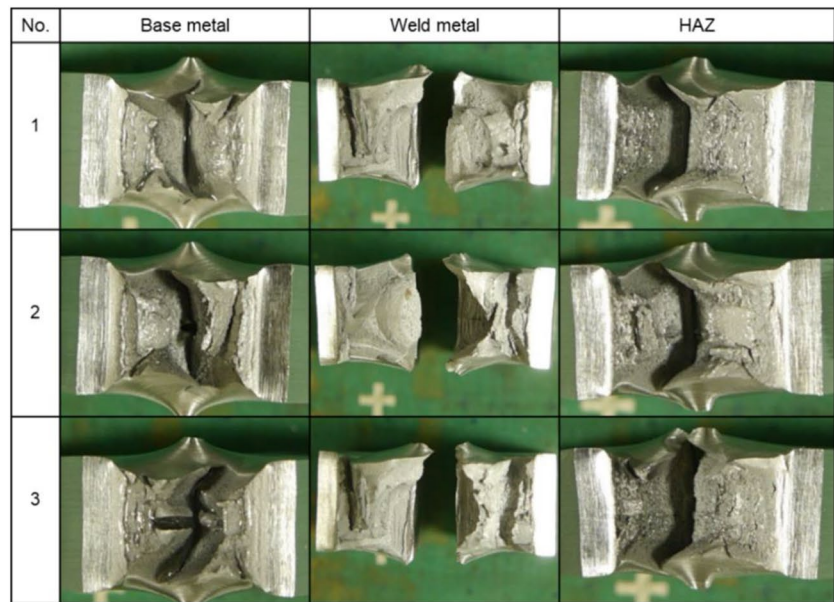
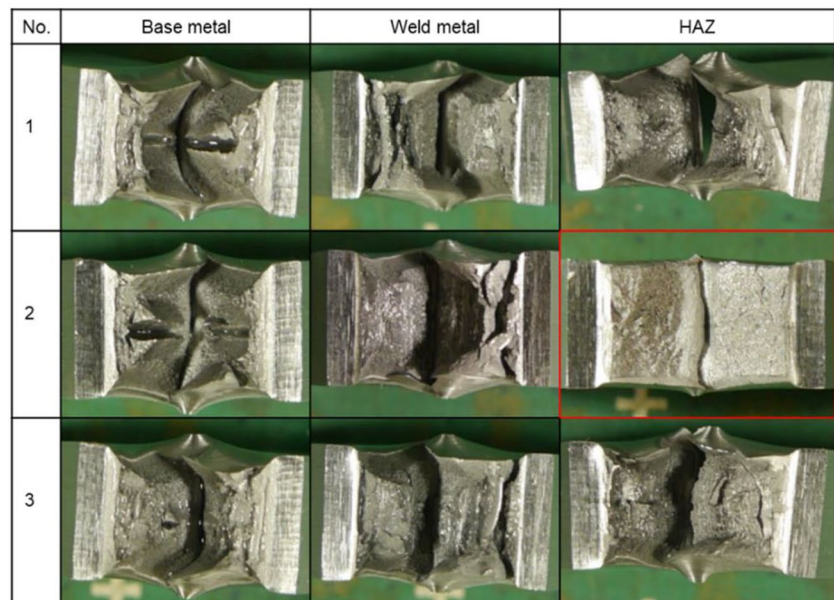


Fig. 6 Results of Charpy impact test. a SBHS400. b SBHS500

### 3.2 Charpy impact test of simulated test piece

#### 3.2.1 Metallographic structures and Vickers hardness test

Figures 8 and 9 illustrate the metallographic structures of the actual HAZ and thermal cycle simulated materials for SBHS400 and SBHS500. Tables 3 and 4 demonstrate the fraction of coarsened metallographic structures. Coarsened metallographic structures were observed in the actual HAZ in regions ① and ② and thermal cycle simulated materials heated to  $1350\text{ }^{\circ}\text{C}$  ( $1350\text{ }^{\circ}\text{C}$  simulated material),  $1200\text{ }^{\circ}\text{C}$  ( $1200\text{ }^{\circ}\text{C}$  simulated material), and  $1050\text{ }^{\circ}\text{C}$  ( $1050\text{ }^{\circ}\text{C}$  simulated material). The fractions of the coarsened metallographic structures for both steel grades of the  $1350\text{ }^{\circ}\text{C}$  and  $1200\text{ }^{\circ}\text{C}$  simulated materials were roughly 100%, with the  $1350\text{ }^{\circ}\text{C}$  simulated materials forming martensite-dominated metallographic structures. The bainite-dominated

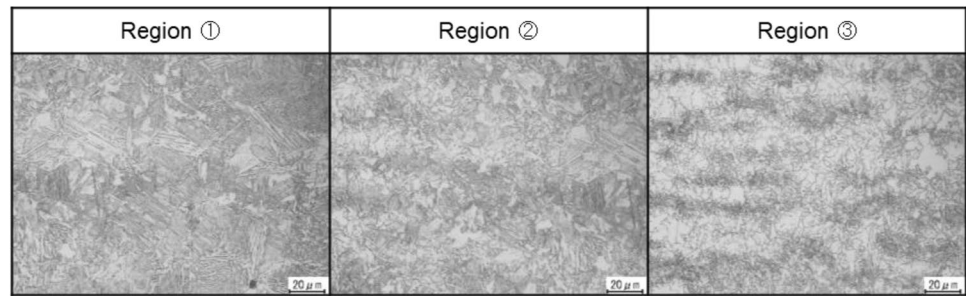
**Fig. 7** Fracture state. **a** SBHS400. **b** SBHS500**(a)****(b)**

microstructures were observed in both the 1200 °C and 1050 °C simulated materials for both steel grades. Regarding the thermal cycle simulated materials at 900 °C (900 °C simulated material), both steel grades did not completely transform to the  $\gamma$  phase under the condition of keeping at 900 °C for 5 s, and no coarsened metallographic structure was observed. Although it is difficult to measure the grain size from the microstructural photographs of region ③ and the 900 °C simulated materials, it can be confirmed that the 900 °C simulated materials had finer grains than region ③ by inspection of the roughness of microstructures.

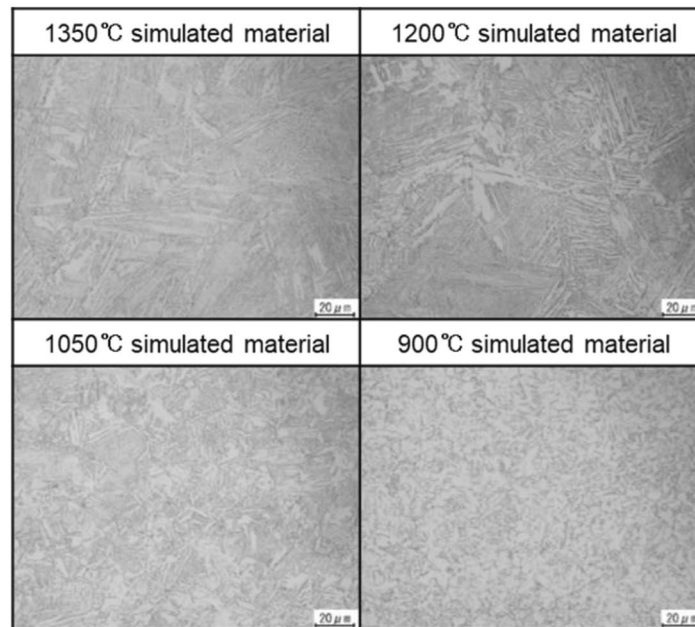
Figure 10 shows the photographs of the metallurgical structure of thermal cycle simulated materials of SM400B. Similar to SBHS400 and SBHS500, the presence of coarsened metallurgical structures (martensite and bainite), which cause a decrease in toughness, was confirmed in the 1350 °C, 1200 °C, and 1050 °C simulated materials. The 1350 °C simulated materials were confirmed to form a 100% martensitic structure. The 1200 °C and 1050 °C simulated materials formed a bainite-dominated microstructure, with the fraction of bainite in the 1200 °C simulated materials large than that in the 1050 °C simulated materials.



**Fig. 8** Simulated thermal cycle test results for SBHS400. **a** Metallographic structure in actual HAZ. **b** Metallographic structure of thermal cycle simulated material



(a)



(b)

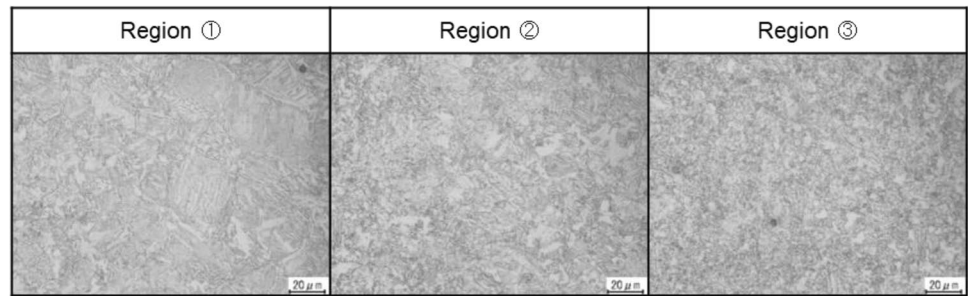
Figure 11 shows the results of the Vickers hardness test. From the SBHS400 results, the hardness of the 1350 °C simulated test pieces is close to that of region ①, the 1200 °C and 1050 °C simulated test pieces to that of region ②, and the 900 °C simulated test pieces to that of region ③. From the SBHS500 results, the hardness of the 1350 °C simulated test pieces is higher than that of region ①, the 1200 °C simulated test pieces to region ① or region ②, the 1050 °C simulated test pieces to region ② or region ③, and the 900 °C simulated test pieces to region ③.

### 3.2.2 Charpy absorbed energy and fracture status of simulated test pieces

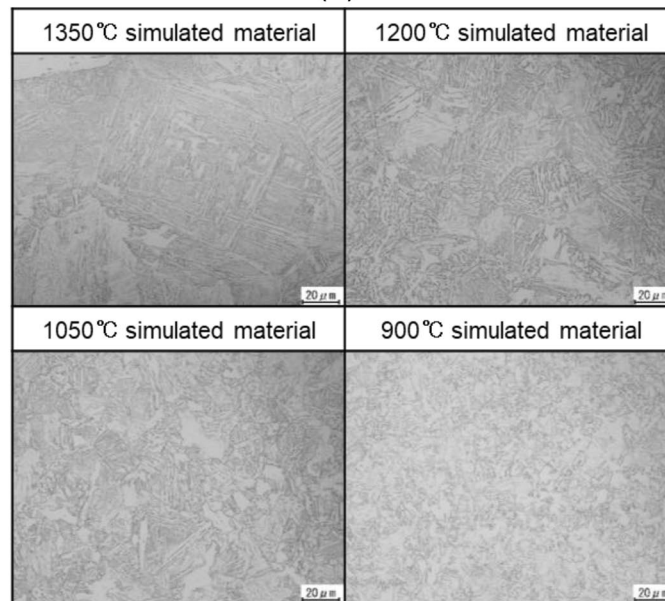
Figure 12 shows the Charpy absorbed energy of each simulated test piece for SBHS400 and SBHS500. The simulated thermal cycle tests formed the same metallographic structures in the vicinity of the notch so that FPD was not observed in all simulated test pieces, and the crack propagated straight ahead from the notch root and ruptured.

Figure 13 demonstrates the fracture status for SBHS400 and SBHS500. The brittle fracture surface ratio of the 900 °C and 1050 °C simulated test pieces was almost 0% for both grades. The brittle fracture surface ratio of the 1350 °C and 1200 °C simulated test pieces was approximately 60% to 80%. The Charpy absorbed energy of the 900 °C simulated test pieces, which was similar to fine-grained HAZ, the 1200 °C simulated test pieces, which was similar to coarse-grained HAZ, and the 1050 °C simulated test pieces, which was similar to the intermediate region between the fine-grained HAZ and coarse-grained HAZ satisfied the 47 J generally required to prevent brittle fracture for both SBHS400 and SBHS500 [18]. Moreover, even in the 1350 °C simulated test pieces whose metallographic structures were coarser than those in the coarse-grained HAZ, the Charpy absorbed energy was 92 J for SBHS400 and 70 J for SBHS500, which was lower than 100 J, a value that guarantees the bending workability of base metals, for both steel grades, but still satisfied 47 J or more.

**Fig. 9** Simulated thermal cycle test results for SBHS500. **a** Metallographic structure in actual HAZ. **b** Metallographic structure of thermal cycle simulated material



(a)



(b)

Figure 14 compares the Charpy absorbed energy of thermal cycle simulated test pieces of SBHS400, SBHS500, and SM400B. Both SBHS and SM400B met their specified values (47 J and 27 J) for 900 °C simulated test pieces, which is similar to fine-grained HAZ, and 1050 °C simulated test pieces, which is similar to the intermediate region

between fine-grained and coarse-grained HAZ. In the case of 1200 °C simulated test pieces similar to coarse-grained HAZ and 1350 °C simulated test pieces with even coarser microstructure than coarse-grained HAZ, the Charpy absorbed energy of SM400B was below 27 J, while that of SBHS400 and SBHS500 met 47 J in the range of this test.

**Table 3** Coarsened fraction of HAZ and thermal cycle simulated test piece for SBHS400

	Actual HAZ			
	Region ①	Region ②	Region ③	
Coarsened metallographic structure fraction (%)	85	23	0	
	Thermal cycle simulated materials			
	1350 degrees simulated materials	1200 degrees simulated materials	1050 degrees simulated materials	900 degrees simulated materials
Coarsened metallographic structure fraction (%)	100	95	70	0

**Table 4** Coarsened fraction of HAZ and thermal cycle simulated test piece for SBHS500

	Actual HAZ		Region ③	
	Region ①	Region ②		
Coarsened metallographic structure fraction (%)	77	17	0	
	Thermal cycle simulated materials			
	1350 degrees simulated materials	1200 degrees simulated materials	1050 degrees simulated materials	900 degrees simulated materials
Coarsened metallographic structure fraction (%)	100	92	68	0

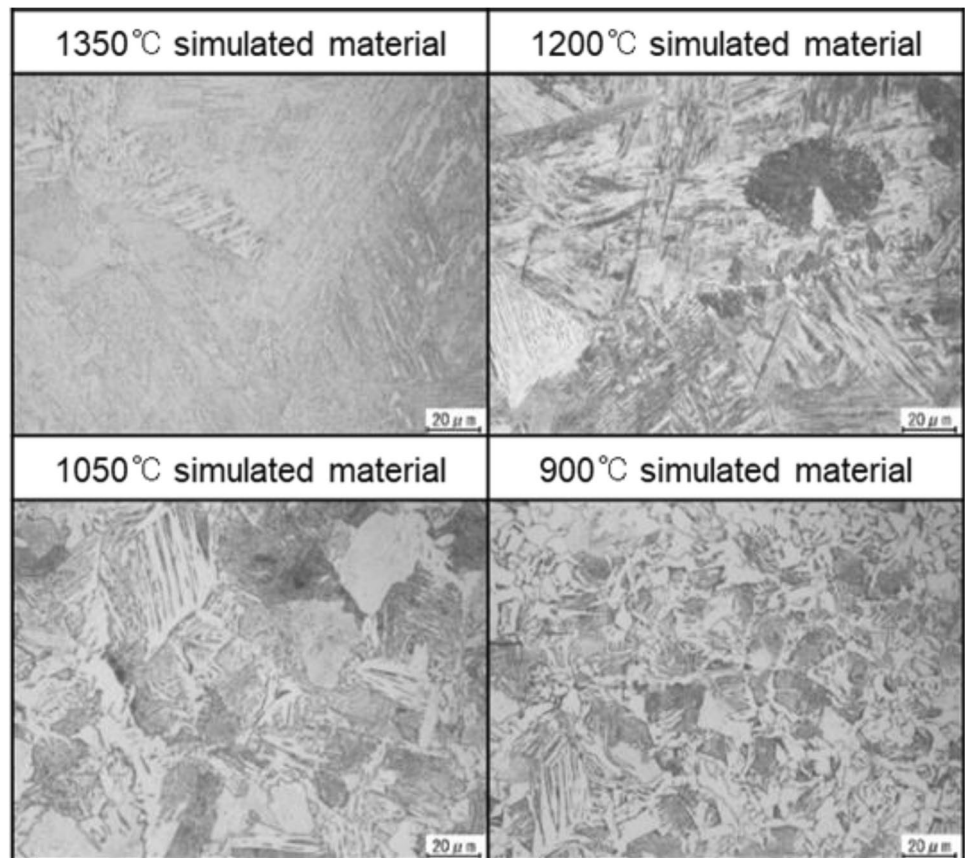
## 4 Discussion

### 4.1 Analysis of Charpy absorbed energy of HAZ

According to the above results mentioned in Sect. 3.1.1 and 3.1.2, the test piece 5H2 might represent the Charpy absorbed energy of the HAZ, where fracture path deviation (FPD) was not observed, and brittle-dominated fracture occurred. As shown in Fig. 3, the hardness of the weld

metal and HAZ was significantly higher than that of the base metal. There is a certain relationship between the hardness and the Charpy absorbed energy [19]. Generally speaking, the higher the hardness of the weld metal and HAZ, the lower the Charpy absorbed energy of them, and the more likely the fracture type is a brittle fracture. Brittle fracture often occurs in a linear way. In other words, the FPD is not prone to occur. However, in this test, FPD occurred in almost all test pieces extracted from the weld metal and HAZ, except test piece 5H2. In addition, a

**Fig. 10** Metallurgical structure of thermal cycle simulated test piece of SM400B. **a** 900 °C simulated test piece. **b** 1050 °C simulated test piece. **c** 1200 °C simulated test piece. **d** 1350 °C simulated test piece



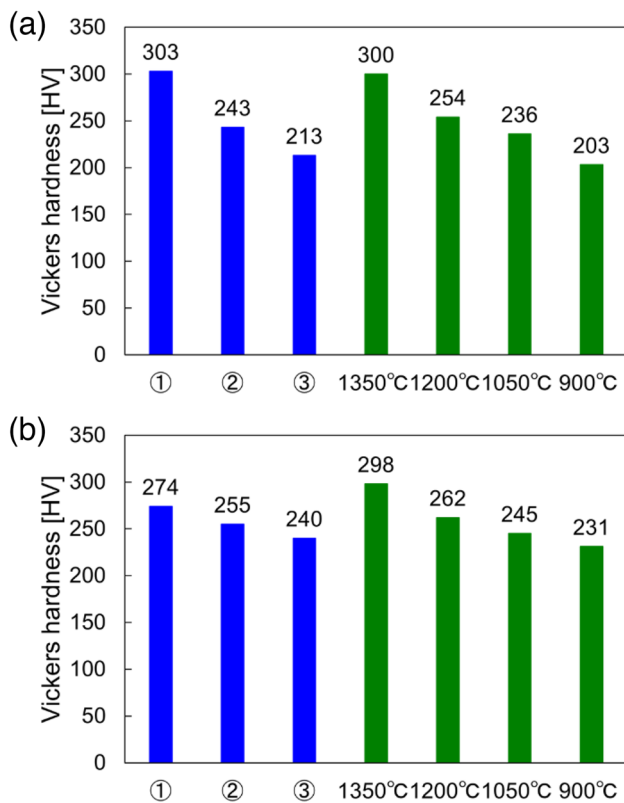


**Fig. 11** Hardness of actual heat-affected zone and thermal cycle simulated test piece. **a** SBHS400. **b** SBHS500

relatively large number of brittle fracture surfaces were observed in test piece 5H2, indicating that brittle-dominated fracture occurred in test piece 5H2. Nevertheless, the brittle fracture surface ratio of other test pieces was almost 0%. This obviously contradicted the theory. Therefore, we considered the Charpy absorbed energy obtained from the test pieces 5H2 as the corresponding Charpy absorbed energy in the HAZ. SBHS features a fine-grained metallurgical structure by the thermo-mechanical control process (TMCP), and brittleness in the HAZ is considered to be reduced compared to conventional steels. However, the rapid heating and cooling by hybrid welding coarsened the metallurgical structures in the HAZ, resulting in a lower Charpy absorbed energy in test piece 5H2 than that in the base metal.

On the other hand, for the test pieces other than test piece 5H2, cracks deviated from the notch root toward the base metal, and then ductile fracture occurred in the base metal. Therefore, the test results might not correspond to the Charpy absorbed energy in the weld metal and HAZ. The weld metal and HAZ of hybrid welded joints are narrow. Moreover, the position of the test pieces may deviate slightly from the center of the support. Hence, it is difficult to determine their local toughness by Charpy impact tests.

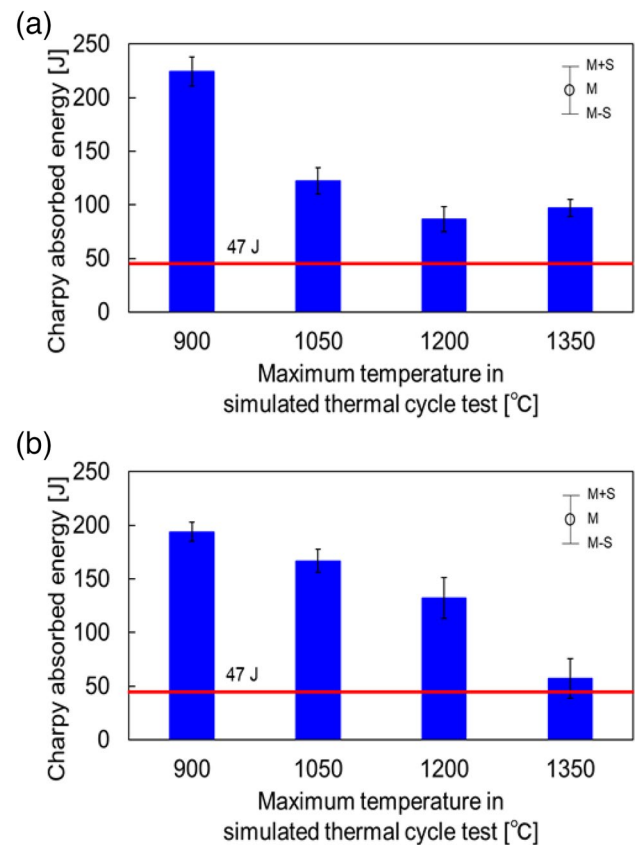


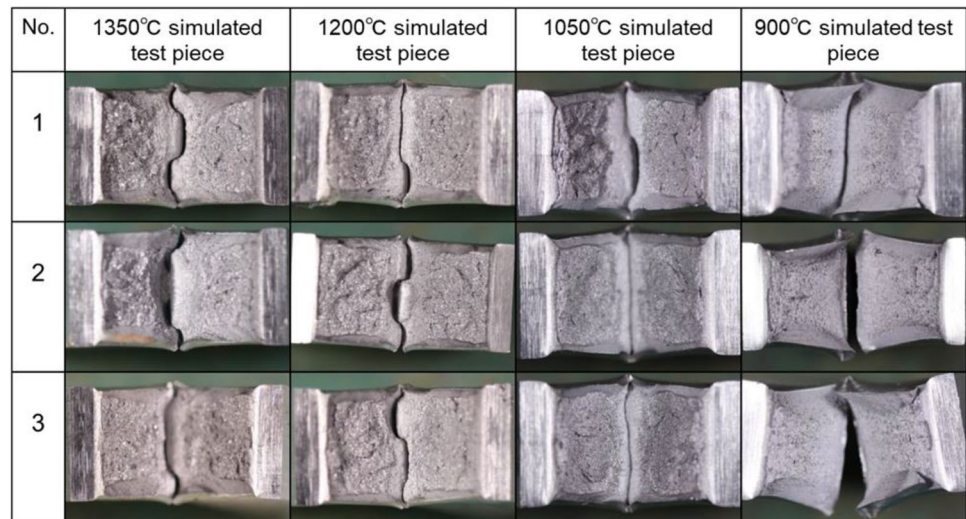
**Fig. 12** Charpy absorbed energy of thermal cycle simulated test piece. **a** SBHS400. **b** SBHS500

In our previous study, the HAZ of hybrid welded joints was as narrow as approximately 1 mm, and material properties such as hardness varied dramatically within this narrow area, making it hard to determine the local toughness by conventional Charpy impact tests [8]. While FPD did not occur only in the test piece 5H2 in this test, the test pieces in the HAZ were more likely to deviate to base metals from the notch roots, instead of going straight, compared to a homogeneous material like the base metal, due in part to the processing accuracy of introducing a V-shaped notch at the center of test pieces in HAZ, where the material properties change significantly.

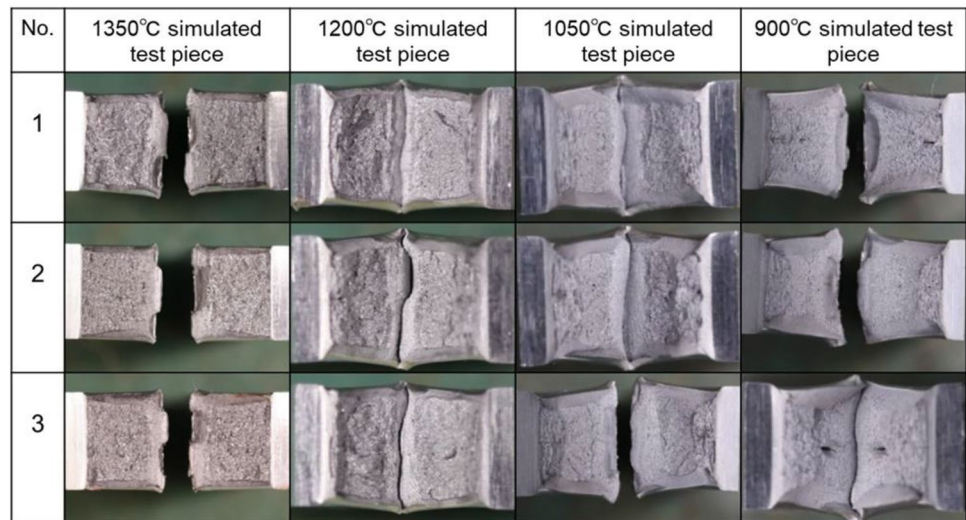
#### 4.2 Metallographic similarity assessment

Rapid cooling creates martensitic and bainitic structures after heating steel materials above the transformation temperature to generate an austenitic structure. Coarsened metallographic structures such as martensite and bainite increase the hardness and decrease the toughness of steel materials, and their fraction is an important indicator of the metallurgical state. Hardness is also a significant index in evaluating the similarity of metallurgical structures.

**Fig. 13** Fracture status. **a** SBHS400. **b** SBHS500



(a)



(b)

Therefore, the metallographic similarity was assessed by the metallographic state and hardness in this study.

For SBHS400, region ① was considered to be the metallographic state between the 1200 and 1350 °C simulated test pieces. The fraction of coarsened metallographic structures of the 1350 °C simulated test pieces was 100% martensite-dominated, whereas region ① was 85% bainite-dominated, which was considered to be more similar to the bainite-dominated 1200 °C simulated test pieces. Region ② was similar to the 1050 °C simulated test pieces in terms of hardness and fraction of coarsened metallographic structures. Although the coarsened metallographic fraction in region ② is lower than that of the 1050 °C simulated test pieces, this was thought to be because the metallographic image in region ② included metallographic features in the region close to

the base metal. According to the metallurgical state and hardness, region ③ was considered to be similar to the metallographic structure of 900 °C simulated test pieces or slightly closer to the HAZ microstructure on the base metal side. As for SBHS500, similar to SBHS400, region ① was considered to be similar to the 1200 °C simulated test pieces, region ② to the 1050 °C material, and region ③ to the 900 °C material. One thousand three hundred fifty degrees Celsius simulated test pieces featured a more coarse-grained metallurgical structure than region ① (coarse-grained HAZ) for both steel grades.

The above analyses indicated that the metallurgical structures of the three HAZs of hybrid weld joints were roughly reproduced by the thermal cycle simulated tests conducted at maximum heating temperatures of 1200 °C, 1050 °C, and 900 °C and a cooling rate of 80 °C/s.

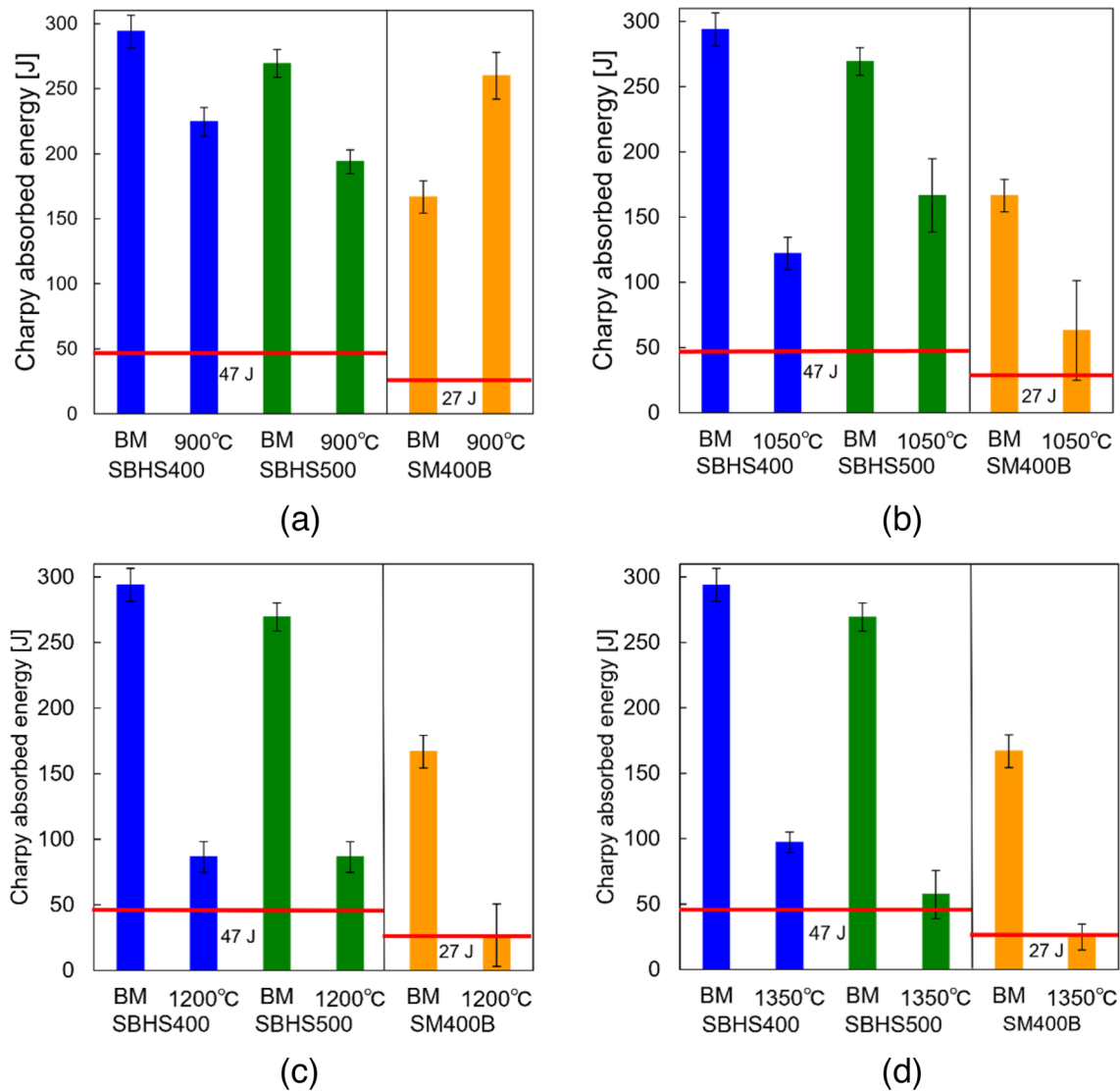


**Fig. 14** Charpy absorbed energy of thermal cycle simulated test piece of SBHS400, SBHS500, and SM400B. **a** 900 °C simulated test pieces. **b** 1050 °C simulated test pieces. **c** 1200 °C simulated test pieces. **d** 1350 °C simulated test pieces

### 4.3 Comparative analysis of SBHS and SM400B

According to the Sect. 3.2.2, FPD did not occur in any of the simulated test pieces, because the uniform metallographic structures were formed near the notch. As a result, Charpy absorbed energy in simulated HAZ was way less than that of actual HAZ. The metallographic structures of the simulated HAZ were coarsened by rapid heating and cooling. This process increased the hardness of simulated HAZ, which might lead to a significant decrease in the Charpy absorbed energy. Nevertheless, the Charpy absorbed energy of all simulated test pieces with SBHS did not fall below 47 J, a criterion for preventing brittle fracture in the range of this test. However, in the case of 1200 °C and 1350 °C simulated

test pieces, the Charpy absorbed energy of SM400B was below 27 J. This is considered to be due to the effective use of the high toughness guaranteed by SBHS. These results suggest that SBHS may ensure high toughness even in the HAZ of hybrid welded joints because of the high absorbed energy in BM.

In this study, the fundamental investigation of the Charpy absorbed energy and the fracture manner of the simulated HAZ specimens of SBHS was conducted. More investigation with fractography characteristics and fracture morphology will be necessary for examining the toughness of the actual hybrid welded joints of SBHS. The relationship between the welding conditions and the fracture manners will be addressed for future work.

## 5 Conclusions

A series of investigations were performed to evaluate the toughness of hybrid welded butt joints using high-yield-point steel plates for bridges. The results obtained are shown below:

- (1) The results of Charpy impact tests on the hybrid welded joints of SBHS showed that FPD occurred in all test pieces except only one test piece in the heat-affected zone. Thus, Charpy absorbed energy in the HAZ and weld metal could not be obtained.
- (2) Simulated thermal cycle tests were performed for reproducing the metallurgical structures of the HAZ of hybrid welded joints. The coarse-grained HAZ, fine-grained HAZ, and mixed microstructure of them were roughly reproduced from the viewpoints of metallographic structure and hardness.
- (3) The results of Charpy impact tests on the thermal cycle simulated test pieces of SBHS showed that the Charpy absorbed energy of the simulated test pieces even with coarse-grained HAZ by the hybrid welding satisfied 47 J generally required to prevent brittle fracture for both steel grades. Moreover, even in the 1350 °C simulated test pieces whose metallographic structures were coarser than those in the coarse-grained HAZ, the Charpy absorbed energy was 92 J for SBHS400 and 70 J for SBHS500, which was lower than 100 J, a value that guarantees the bending workability of base metals.
- (4) By comparing the Charpy absorbed energy of SBHS and SM400B, both SBHS and SM400B met their specified values (47 J and 27 J) for 900 °C and 1050 °C simulated test pieces. In the case of 1200 °C and 1350 °C simulated test pieces, the Charpy absorbed energy of SM400B was below 27 J, while that of SBHS400 and SBHS500 met 47 J in the range of this test. These results suggested that SBHS may ensure high toughness even in the HAZ of hybrid welded joints because of the high absorbed energy in BM.

In this paper, the FPD and brittle fracture surface ratio were two significant indicators to assess the fracture characteristics of test pieces of SBHS, which facilitated the evaluation of the toughness of hybrid welded butt joints using SBHS. Toughness is essential for steel bridges, which are subjected to dynamic loadings such as earthquake and wind loads, and if they lack sufficient toughness, fracture may occur under these loading conditions. Therefore, it is crucial to elucidate the in-depth mechanism of the toughness behavior by taking into consideration more indicators such as fractography and micro viewpoints in the future.

**Author contribution** The manuscript was written through the contributions of all authors. Mr. G. Chen and Ms. N. Sakai performed the experiment and analyzed the results. They described the paper. Mr. K. Hyoma and Mr. N. Matsumoto prepared and processed the experimental specimens. Dr. M. Hirohata and Dr. K. Inose planned and led the research.

**Funding** Open access funding provided by Osaka University. This research was supported by a grant from the Japan Iron and Steel Federation (JISF) and JST SPRING, Grant Number JPMJSP2138.

## Declarations

**Conflict of interest** The authors declare no competing interests.

**Open Access** This article is licensed under a Creative Commons Attribution 4.0 International License, which permits use, sharing, adaptation, distribution and reproduction in any medium or format, as long as you give appropriate credit to the original author(s) and the source, provide a link to the Creative Commons licence, and indicate if changes were made. The images or other third party material in this article are included in the article's Creative Commons licence, unless indicated otherwise in a credit line to the material. If material is not included in the article's Creative Commons licence and your intended use is not permitted by statutory regulation or exceeds the permitted use, you will need to obtain permission directly from the copyright holder. To view a copy of this licence, visit <http://creativecommons.org/licenses/by/4.0/>.

## References

1. Elmesalamy A, Francis J, Li L (2014) A comparison of residual stresses in multi pass narrow gap laser welds and gas-tungsten arc welds in AISI 316L stainless steel. *Int J Press Vessels Pip* 113:49–59. <https://doi.org/10.1016/j.ijpvp.2013.11.002>
2. Katayama S, Kawahito Y, Mizutani M (2010) Elucidation of laser welding phenomena and factors affecting weld penetration and welding defects. *Phys Procedia B* 5:9–17. <https://doi.org/10.1016/j.phpro.2010.08.024>
3. Uemura T, Gotoh K, Uchino I (2022) Expansion of laser–arc hybrid welding to horizontal and vertical-up welding. *Weld. World* 66:495–506. <https://doi.org/10.1007/s40194-021-01236-7>
4. Acherjee B (2018) Hybrid laser arc welding: State-of-arc review. *Opt Laser Technol* 99:60–71. <https://doi.org/10.1016/j.optlastec.2017.09.038>
5. Gogolukhina M, Mamedova L, Scholtz O, Firsova A (2019) Feasibility study of hybrid laser arc welding application in shipbuilding. *Key Eng Mater* 822:459–466. <https://doi.org/10.4028/www.scientific.net/KEM.822.459>
6. Hirohata M, Takeda F, Suzaki M, Inose K, Matsumoto N, Abe D (2019) Influence of laser-arc hybrid welding conditions on cold cracking generation. *Weld. World* 63:1407–1416. <https://doi.org/10.1007/s40194-019-00749-6>
7. Koga H, Goda H, Terada S, Hirota K, Nakayama S, Tsubota S, First application of hybrid laser-arc welding to commercial ships, Mitsubishi Heavy Industries Technical Review. 47 (2010) 59–64. <https://www.mhi.co.jp/technology/review/pdf/e473/e473059.pdf>.
8. Hirohata M, Chen G, Morioka K, Hyoma K, Matsumoto N, Inose K (2022) An investigation on laser-arc hybrid welding of one-pass full-penetration butt-joints for steel bridge members. *Weld. World* 66:515–527. <https://doi.org/10.1007/s40194-021-01221-0>

9. Yokozeki K, Miki C, Suzuki K (2011) Optimum design of I-girder bridges using high performance steel. *J Struct Eng* 18:15–25. [https://doi.org/10.11273/jssc.18.71\\_15](https://doi.org/10.11273/jssc.18.71_15). (in Japanese)
10. Nozaka K, Okui Y, Komuro M, Miyashita T, Nogami K, Nagai M (2013) Experimental study on the strength of SBHS I-girder. *J Struct Eng* 59A:70–79. <https://doi.org/10.11532/structcivil.59A.70>. (in Japanese)
11. Hirohata M, Sakai N, Morioka K, Matsumoto N, Hyoma K, Inose K (2020) Application of laser-arc hybrid welding to thick steel plates for bridge structures, Vehicle and Automotive. *Engineering* 3:489–496. [https://doi.org/10.1007/978-981-15-9529-5\\_42](https://doi.org/10.1007/978-981-15-9529-5_42)
12. Ohata M, Morimoto G, Fukuda Y, Minami F, Inose K, Handa T (2015) Prediction of ductile fracture path in Charpy V-notch specimen for laser beam welds. *Weld. World* 59:667–674. <https://doi.org/10.1007/s40194-015-0256-x>
13. Kim Y-C, Lee J-Y, Inose K (2010) Determination of dominant factors in high accuracy prediction of welding distortion. *Weld World* 54(7/8):234–240. <https://doi.org/10.1007/BF03263509>
14. Takashima Y, Ohata M, Inose K, Yamaoka H, Nakanishi Y, Minami F (2016) Evaluation of Charpy impact toughness using side-grooved specimen for hybrid laser-arc welds of ultra-high-strength steel. *Weld. World* 60:1191–1199. <https://doi.org/10.1007/s40194-016-0383-z>
15. Inose K, Yamaoka H, Nakanishi Y, Minami F (2017) Toughness assessments of laser arc-hybrid welds of ultra-high strength steel. *Weld. World* 61:955–961. <https://doi.org/10.1007/s40194-017-0483-4>
16. Wei H, Blecher J, Palmer T, Debroy T (2015) Fusion Zone Microstructure and geometry in complete-joint-penetration laser-arc hybrid welding of low-alloy steel. *Weld J* 94:135–144
17. Chen J, Zhang Z, Zhang Z, Liu Y, Zhao X, Chen J, Chen H (2022) Effect of the cooling rate of thermal simulation on the microstructure and mechanical properties of low-carbon bainite steel by laser-arc hybrid welding. *Coatings* 12(8):1045. <https://doi.org/10.3390/coatings12081045>
18. Japan Welding Engineering Society (1995) WES3003 Evaluation criterion of rolled steels for low temperature application. The Japan Welding Engineering Society, Tokyo
19. Wang X, Chen Y, Wei S, Zuo L, Mao F (2019) Effect of carbon content on abrasive impact wear behavior of cr-si-mn low alloy wear resistant cast steels. *Front Mater* 6:153. <https://doi.org/10.3389/FMATS.2019.00153>

**Publisher's note** Springer Nature remains neutral with regard to jurisdictional claims in published maps and institutional affiliations.